GEOPHYSICS, VOL. 72, NO. 2 (MARCH-APRIL 2007); P. WA39–WA49, 11 FIGS.
10.1190/1.2434775

Downloaded 09/23/13 to 128.83.63.20. Redistribution subject to SEG license or copyright; see Terms of Use at http://library.seg.org/

Special Section — Marine Controlled-Source Electromagnetic Methods

Marine downhole to seafloor dipole-dipole electromagnetic methods and the resolution of resistive targets

Carsten Scholl[1] and R. Nigel Edwards[1]

ABSTRACT

Most active marine electromagnetic surveys use an array of transmitting and receiving electric dipoles located on the seafloor. There are many reports of successful detections of buried resistors with these arrays. Nevertheless, the concept has a significant drawback: Large offsets between the transmitter and receiver with respect to the target depth are needed. A logical alternative is the use of a vertical electric-dipole transmitter in a borehole deeper than the target, combined with receivers located at the seafloor. Because current must pass through the target, even data recorded at short offsets with respect to target depth should be sensitive to the target. We derived the equations for the electric and magnetic field components produced by the vertical electric dipole in a 1D layered medium. The equations are used to model the fields for resistive layers. An eigenparameter analysis is applied to the different field components, and the resolution is compared with the standard seafloor inline array. The analyses show that data for the downhole transmitter are more sensitive to the resistance between the source and the receiver than the seafloor array. However, model geometry such as depth to the target is resolved less easily. The resolution of the model geometry is improved significantly when a long bipole transmitter is used, extended from below the target layer to a level above it. We carried out 3D modeling for the downhole transmitter through the use of a finite-difference algorithm. Results indicate that these data are very sensitive to lateral changes within the target layer. Differences between electric fields simulated at the seafloor for 3D models and a reference model show a correlation to lateral resistivity differences. This finding suggests that the array is suitable for mapping and monitoring resistivity anomalies outward from the borehole.

INTRODUCTION

Resistive hydrocarbons such as oil, gas, and gas hydrate increase formation resistivity of sedimentary layers by filling or blocking pore space that otherwise would be filled with more conductive pore water: The higher the electrical resistivity, the greater the volume fraction of hydrocarbons. Marine controlled-source electromagnetic methods (CSEM) allow derivation of resistivity distribution below the seafloor (Chave et al., 1991). Cheesman et al. (1987) argue that hydrocarbons can be detected with electrical methods more directly than with widely used seismic methods. There are many recent success stories (Ellingsrud et al., 2002; Amundsen et al., 2004; Schwalenberg et al., 2005; MacGregor et al., 2006; Srnka et al., 2006; Weitemeyer et al., 2006).

Typically, marine electromagnetic measurements are made by recording horizontal components of the electric field produced by a rectangular current function in a horizontal electric-transmitting dipole. The transmitter (TX) and the receivers (RX) are located at or near the seafloor. Data are collected along a profile either by towing the TX along a line of stationary RX units (Constable and Cox, 1996) or dragging the complete TX-RX array over the seafloor (Yuan and Edwards, 2000).

Abrupt current changes in the TX dipole induce current systems, which diffuse away from the TX. They are recorded at the RX units as functions of time after the change of state in the TX. The target resolution for marine CSEM depends on the time channel or frequencies at which data are recorded and the TX-RX offset. The resolution of a deeper target requires larger offsets and lower frequencies

Manuscript received by the Editor May 17, 2006; revised manuscript received October 6, 2006; published online March 1, 2007.
[1]University of Toronto, Department of Physics, Toronto, Ontario, Canada. E-mail: cscholl@physics.utoronto.ca; edwards@core.physics.utoronto.ca.
© 2007 Society of Exploration Geophysicists. All rights reserved.

Downloaded 09/23/13 to 128.83.63.20. Redistribution subject to SEG license or copyright; see Terms of Use at http://library.seg.org/

or later times (Edwards, 1988; Chave et al., 1991). The correlation between TX-RX offset and exploration depth is an important drawback because (1) the signal decays with offset, i.e., very deep targets may require large offsets at which the signal is not detectable, and (2) it is not easy to separate lateral from vertical resistivity variations, because changes in data with offset could indicate lateral and vertical changes in resistivity. A separation of vertical and lateral effects thus requires several different TX/RX positions, which hampers monitoring with a stationary array.

To overcome the drawbacks of the seafloor system, we examine the possibility of using a configuration in which a vertical electric dipole in a borehole is used as a source. If the transmitting dipole is located below the target, the induced current systems have to diffuse through the resistive target layer to reach the RX located at the seafloor. Recorded data should be influenced by the target layer even at small horizontal offsets.

We propose to deploy the system within the framework of the Integrated Ocean Drilling Program (IODP), which will drill holes in some of the hydrate structures at the Cascadia margin, offshore Vancouver Island, Canada (Riedel et al., 2002; Schwalenberg et al., 2005), in the near future. Hence, the depth and thickness of the resistive targets used in this paper are scaled to a few hundreds meters, consistent with the geometry of the methane hydrate layer found in the area. For applications to deeper resistive targets like oil and gas, TX-RX separations and time windows would have to be increased. The main experimental problem then becomes measurement of weaker signals.

We present a method of calculating the electric and magnetic fields produced by a vertical electric dipole embedded in a horizontally layered (1D) medium. The 1D calculation is used to infer the resolution properties of the configuration for different field components and offsets in comparison with the standard seafloor system. Subsequently, a 3D code is used to examine the resolution of lateral changes with a downhole TX, including some easy ways of deriving a quantitative resistivity structure from multidimensional data sets.

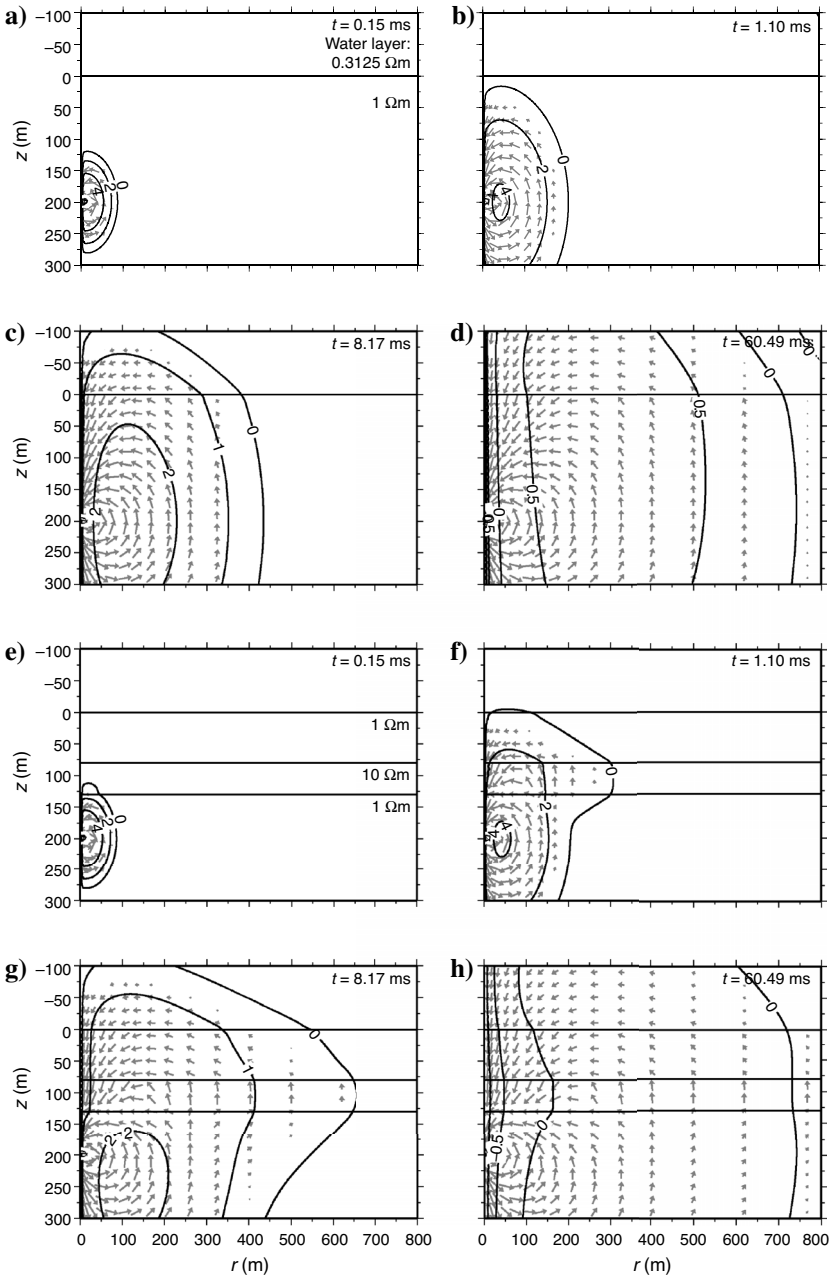


Figure 1. Evolution of the switch-on fields for a downhole E_z-TX for two different models.

LAYERED MODELS

We show fields produced by a vertical-electric dipole transmitter embedded in a layered medium. The algorithm for computing these fields is described in Appendix A. The term *unit dipole* will be used for dipoles with a length of 1 m in which the current is switched from 0 to 1 A. In the 1D layered case, only the radial and vertical electric field components E_r and E_z and the tangential magnetic B_ϕ component are excited.

We also compare behavior of the field for the vertical TX dipole to the standard inline electric dipole-dipole array, i.e., the ERER array described in Cheesman et al. (1987). In the following comparisons, the corresponding component calculated for an inline electric system on the seafloor is called E_x.

Field systems of a vertical electrical dipole at depth

Figure 1 shows the evolution of the electric field system and the time derivative of the magnetic field $\dot{B}_\phi$ after switching on a z-directed unit dipole at a depth of 200 m below seafloor (mbsf). In Figure 1a-d, resistivity of the earth below the seafloor and the water is 1 and 0.3125 Ωm, respectively. The water layer is 1300 m thick, so at the offsets shown in the plots, the fields are not influenced by the air layer. Contoured are isolines

Downloaded 09/23/13 to 128.83.63.20. Redistribution subject to SEG license or copyright; see Terms of Use at http://library.seg.org/

of $\log_{10}(\dot{B}_\phi)$, where $\dot{B}_\phi$ is measured in picoteslas per second. We choose to plot the time derivative instead of B_ϕ because coils typically would be used to measure the magnetic components. The gray arrows show the direction of the electric fields. The length of the arrows indicates the strength of the electric field. The E_z component is discontinuous at the layer boundary. For the plot, the E_z value just below the boundary is used for displaying the arrows at boundaries.

At early times, the fields are concentrated around the TX, and they spread out with increasing time. At later times, only minor changes in the vicinity of the TX can be observed, while significant changes occur at larger offsets. When the perturbed fields reach the seafloor ($z = 0$ m), they also start to diffuse through the water layer. The diffusion speed there, however, is slower because of higher conductivity, producing a sharp discontinuity in the gradient of the $\dot{B}_\phi$ isolines at the seafloor. At all times, the electric field arrows point inward for $z < 200$ m and outward for $z > 200$ m. Thus, an E_r transient shows no sign reversals. Measured at the seafloor, E_r is negative for all times. The same is true for $\dot{B}_\phi$. In contrast, E_z can exhibit sign reversals, depending on the offset. For the times and the model shown in Figure 1, the E_z component at the seafloor is strictly positive at offsets smaller than 100 m. At offsets larger than 300 m, E_z is negative. In between, the transients exhibit a sign reversal. Here, E_z is negative for early times and positive for later times.

In Figure 1e-h, the same TX geometry is used, but a resistive 10-Ωm, 50-m-thick layer is embedded 80 mbsf. The fields are significantly distorted by the inhomogeneity. The field disturbance enters the resistive zone and diffuses laterally in the layer significantly faster than in the surrounding 1-Ωm material. Disturbance in the layer produces fields similar to seismic head waves in the host medium. Through the lobes of this V-shaped structure, the field systems reach the seafloor faster than they would otherwise. In the lower part of the structure, the E_r component has a sign opposite to that of the primary field. The E_r transients at these depths exhibit sign reversals.

The vertical dipole does not excite a so-called airwave, which for the standard inline array, appears at offsets significantly larger than the water depth. Figure 2 shows transients for an electric horizontal sensor using a horizontal or vertical unit dipole. The horizontal TX is located on the seafloor, the vertical dipole 5 mbsf. Transients are calculated for a TX-RX offset of 1.5 km. The lower half-space has a resistivity of 1 Ωm, and the water has a conductivity of 3.2 S/m. Arrival times for the standard array change significantly in the shallow-water case (Figure 2a) because the path through the water and the air layer is faster for this setup. For the vertical dipole TX, the shape of the transients at early times does not change. Here, interpretation of arrival time would still lead to the same result.

The fields at the seafloor

Field disturbances produced by a downhole TX diffuse up through the resistive layer to any seafloor RX, whereas for inline systems, the fields must first diffuse downward to reach the target. Thus, the part of the field diffusing through the upper, more conductive part of the seafloor will reach the RX at smaller offset faster than the resistive target layer. However, upon reaching the layer, the disturbance will diffuse in it similarly to the example shown in Figure 1. Beyond a certain offset, the part diffusing through the resistive layer will reach the receivers faster than the disturbance traveling through the more conductive part.

Edwards (1997) proposed to interpret marine CSEM data by using arrival times at various RX sites. He defines arrival times as the first maximum of the step response, differentiated with respect to logarithmic time, i.e., $\partial E_x(t)/\partial \log t$. Figure 3 shows step-on response (solid line) for an inline setup at the seafloor with TX-RX offset of 273 m for a three-layer case (80-m-thick 1-Ωm layer and a 50-m-thick 10-Ωm layer over a 1-Ωm half-space) under an infinitely thick water layer of 3.2 S/m. The dashed line, showing $\partial E_x(t)/\partial \log t$, exhibits two distinct maxima. The first is produced by fields diffusing through more resistive subsoil; the second marks the arrival of the fields in the sea layer.

Figure 4 shows these log-time differentiated step-on responses for different TX-RX and model geometries. The wiggle traces represent the curves for E_x-RX with offsets between 50 and 5000 m. The graphs are normalized with respect to their maximal absolute value. Each panel shows two different sets of curves. In Figure 4a, b, and d, the filled wiggles (gray) show the curves for a water layer (3.2 S/m)

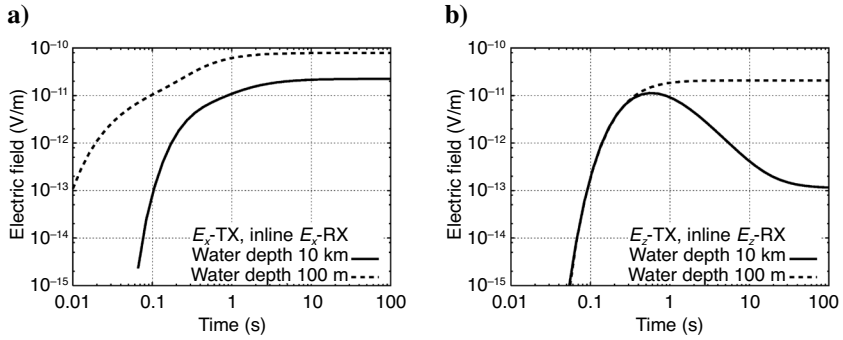


Figure 2. (a) E_x transients for a standard seafloor inline system and (b) the radial E_r component produced by a vertical electric TX for thick (solid) or thin (dashed) water layers.

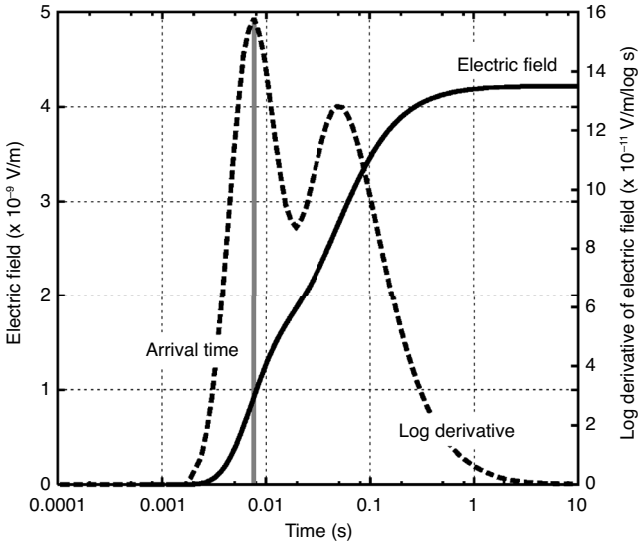


Figure 3. Step-on response (solid black) and its derivative with respect to logarithmic time (dashed) for the standard seafloor inline array for a three-layer case (1, 10 Ωm, thicknesses 80 and 50 m, respectively, over a 1-Ωm half-space, offset 273 m).

Downloaded 09/23/13 to 128.83.63.20. Redistribution subject to SEG license or copyright; see Terms of Use at http://library.seg.org/

over a 1-Ωm half-space, and the black lines denote results for the same three-layer model used in Figure 3. In Figure 4c, the curves are compared for the two different TX configurations and the three-layer models.

Figure 4a shows curves for the standard seafloor inline array. For the half-space (gray), connecting the first maximum of each curve yields a straight line. Connecting the second maxima would yield another parallel line (dashed lines). Both have a slope close to two, signifying that the arrival time is proportional to the square of the separation for a model of nearly constant conductivity (Edwards, 1997). The first maximum is not very pronounced because of the low resistivity contrast between the half-spaces.

At small offsets, the curves in Figure 4a for the three-layer case (black) are identical to those for the half-space model. At an offset of 200 m (log offset ≈ 2.3 in the diagram), the current diffusing through the deeper, resistive layer arrives earlier at the receivers. The slope of the curve connecting the first maxima decreases until at an offset of around 1000 m, the slope changes back to two. Edwards (1997) used this effect to resolve the parameters of the subseafloor model by inverting arrival times versus offset curves for resistivity models.

Figure 4b shows curves for the same models as Figure 4a and a unit E_z-TX at a depth of 5 mbsf. The shape of the curves changes. Instead of two maxima, the curves show a maximum and a minimum because in this case, the extremal points associated with the fields diffusing through water and sediments have opposite signs. Similar to the seafloor E_x-TX case, the resistive layer manifests itself in earlier first arrivals beyond intermediate offsets. In fact, the first arrival times are identical (Figure 4c).

Figure 4d shows curves for a downhole E_z-TX below the resistive layer at a depth of 200 m. Because of the different geometry, the first arrivals describe a hyperbolic-shaped curve. Beyond 100 m, the first arrival times are similar to those for the previous TX geometries.

When the resistive layer is included, the fields must also penetrate this resistor to reach the receivers at very small offsets. The arrival time is shifted to smaller values even for the closest receivers. Hence, it is possible to detect anomalous resistivities regardless of offset. The effects of lateral and vertical resistivity changes thus are less coupled, which should improve the resolution of lateral variations.

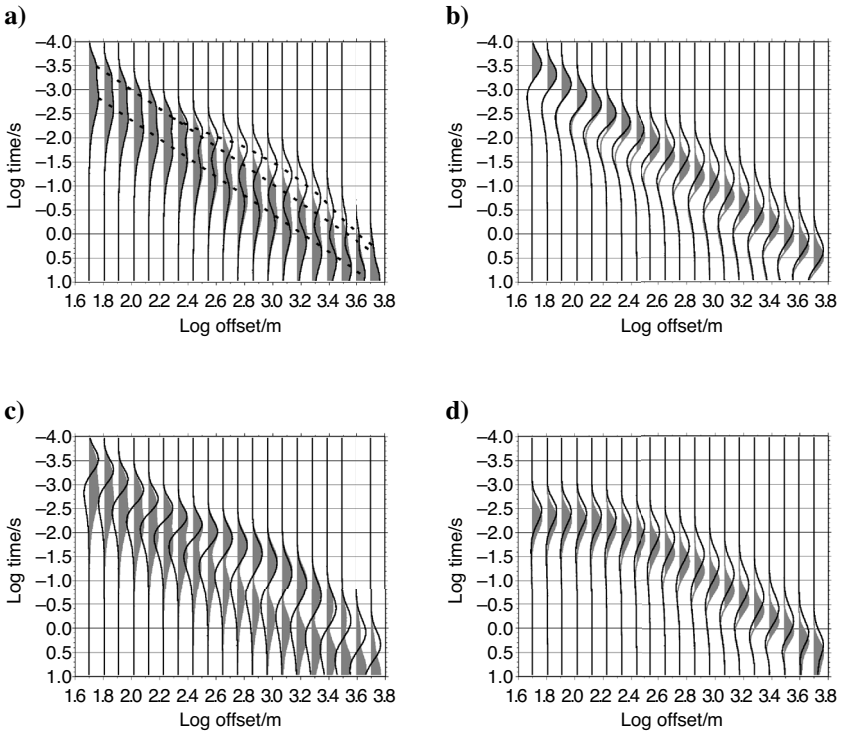


Figure 4. Step-on responses differentiated with respect to logarithmic time for different TX geometries and models. (a) Unit E_x-dipole TX at seafloor, two half-spaces (black), three-layer model (gray). (b) Unit E_z-dipole TX at a depth of 5 m, two half-spaces (black), three-layer model (gray). (c) Comparison between the three-layer curves from (a) and (b). (d) Unit E_z-dipole TX at a depth of 200 m, two half-spaces (black), three-layer model (gray). The polarity of curves for the E_z dipole is changed. The models are described in the text.

Resolution of a resistive target layer

Although the current system of a TX below the target has to diffuse through it to get to RXs at the seafloor, it is not clear how well the relevant model parameters can be derived from the data sets. We examine the resolution properties of the downhole array and compare them with the performance of the standard inline seafloor array by using a linear eigenparameter analysis (Jupp and Vozoff, 1992; Raiche et al., 1985) applied to synthetic data.

Suppose a model is described by a parameter vector $\mathbf{m}$ with M entries. Let $\mathbf{f}(\mathbf{m})$ be the N-dimensional data vector matching the model. For small perturbation of the model parameters $\boldsymbol{\delta}\mathbf{m}$, the change in the data vector $\boldsymbol{\delta}\mathbf{f}$ can be described by the first-order term of a Taylor series as

$$\boldsymbol{\delta}\mathbf{f} = \mathbf{J}\boldsymbol{\delta}\mathbf{m}, \tag{1}$$

where $\mathbf{J}$ is the Jacobian or sensitivity matrix containing the partial derivatives

$$J_{ij} = \frac{\partial f_i(\mathbf{m})}{\partial m_j}, \quad i = 1, \ldots, N, \quad j = 1, \ldots, M. \tag{2}$$

$\mathbf{J}$ contains the information on how the data are changed by small changes of the model. The content of the Jacobian can be studied effectively by using a singular-value decomposition (SVD) to find a different representation of $\mathbf{J}$ as a product of three matrices

$$\mathbf{J} = \mathbf{U}\mathbf{S}\mathbf{V}^T. \tag{3}$$

$\mathbf{U}$ and $\mathbf{V}$ are $N \times M$ and $M \times M$ matrices, respectively, with

$$\mathbf{U}^T\mathbf{U} = \mathbf{V}^T\mathbf{V} = \mathbf{V}\mathbf{V}^T = \mathbf{I}, \tag{4}$$

where $\mathbf{I}$ is the $M \times M$ identity matrix. $\mathbf{S}$ is an $M \times M$ diagonal matrix, containing eigenvalues of $\mathbf{J}$. The matrix $\mathbf{V}$ contains the so-called eigenparameters (EPs), with which we analyze in detail which combination of the original model parameter can be resolved by the data.

Equation 1 is a good approximation for changes in the model response $\mathbf{f}$ only when they depend linearly on $\mathbf{m}$. For TEM applications, this is only

Downloaded 09/23/13 to 128.83.63.20. Redistribution subject to SEG license or copyright; see Terms of Use at http://library.seg.org/

the case for very small perturbations of **m**. Typically, both **m** and **f** are transformed logarithmically because in transformed space, the dependency of **f** on **m** is closer to linear. However, because the E_z transients exhibit sign reversals, we can not simply transform our data sets logarithmically to calculate the relative differences. Instead, we will use an area sine hyperbolic (arsinh) transform

$$\tilde{f}_i = \operatorname{arsinh} f_i/s = \ln(f_i/s + \sqrt{(f_i/s)^2 + 1}) \qquad (5)$$

for **f**, which shows a logarithmical behavior if the datum f_i is much larger than the scaling parameter s or much smaller than $-s$. The scaling parameter is set to 1% of the maximal absolute value of the transient **f**. With these two transformations, the entries of the transformed Jacobian are

$$\tilde{J}_{ij} = \frac{\partial \tilde{f}_i}{\partial \log m_j} = \left(\frac{\partial \log m_i}{\partial m_i}\right)^{-1} \frac{\partial \tilde{f}_i}{\partial f_i}\frac{\partial f_i}{\partial m_j} = \frac{m_j}{\sqrt{f_i^2 + s^2}}\frac{\partial f_i}{\partial m_j} \qquad (6)$$

for $i = 1,\ldots,N$ and $j = 1,\ldots,M$.

Figure 5 shows the results of the eigenparameter analysis for the three-layer case that was used previously ($\rho_1 = \rho_3 = 1$ Ωm, $\rho_2 = 10$ Ωm, $d_1 = 80$ m, $d_2 = 50$ m; see Figure 1). Transients were calculated for 40 logarithmically equispaced data points between 0.1 ms and 3 s. Jacobians were calculated for unit dipoles and three RXs at the seafloor at TX-RX offsets of 50, 300, and 900 m (Figure 5a, b and c, respectively) and a unit inline TX at the origin (E_x component). Figure 5d-f shows the results for the same RX positions but for a downhole E_z-TX at a depth of 200 m below the seafloor.

Displayed are entries of the eigenparameter (EP) matrix **V** and corresponding eigenvalues (EV) from **S**. EVs give a measure for the importance of an eigenparameter. Depending on the S/N, the eigenparameters with eigenvalues larger than a certain value can be resolved. We consider EPs with associated EVs < 15 as not resolvable. Of course, it is easier to resolve an EP when its eigenvalue is larger. EPs are sorted with respect to their eigenvalues. EP1 and EP5 are the most and least important eigenparameters, respectively. Each column shows the composition of one EP.

For the closest E_x-RX at $x = 50$ m (Figure 5a), the first EP consists only of ρ_1. Thus, it should be possible to resolve this model parameter very well. The next EP is dominated by d_1, but its EV is small. All other parameters are represented in EPs with much smaller EVs, hindering their resolution. The matrix **V** has a different structure for the E_x-RX at $x = 150$ m (Figure 5b). Here, the first EP consists mainly of a combination of ρ_1 and d_1, namely $\rho_1^{V_{11}} d_1^{V_{41}}$. V_{41} is negative, so it should be possible to resolve ρ_1/d_1. EP2 mainly represents $\rho_1 d_1$, so with these two EPs, ρ_1 and d_1 can be resolved independently. EP3 represents a mixture of ρ_2 and ρ_3, so the data are influenced by deeper structures. To resolve these parameters independently, however, EP4 and EP5 are needed, but their EVs are small. The structure of the **V** matrix for the last E_x-RX at $x = 900$ m (Figure 5c) is also different. The EVs decay less, and the EPs consist more of combinations of the individual parameters. Hence, it might be hard to resolve the different model parameters independently. The least important EP mainly represents ρ_1. Other parameters are represented in the more important EPs. Thus, the data set is more sensitive to the deeper structure.

With the combined data sets, the resistivity model is well resolved because the structure of the EP changes with increasing offset. For example, ρ_1 can be derived from the short offsets, which reduces the ambiguity at larger offsets. However, this requires that only minor lateral changes in resistivity are present.

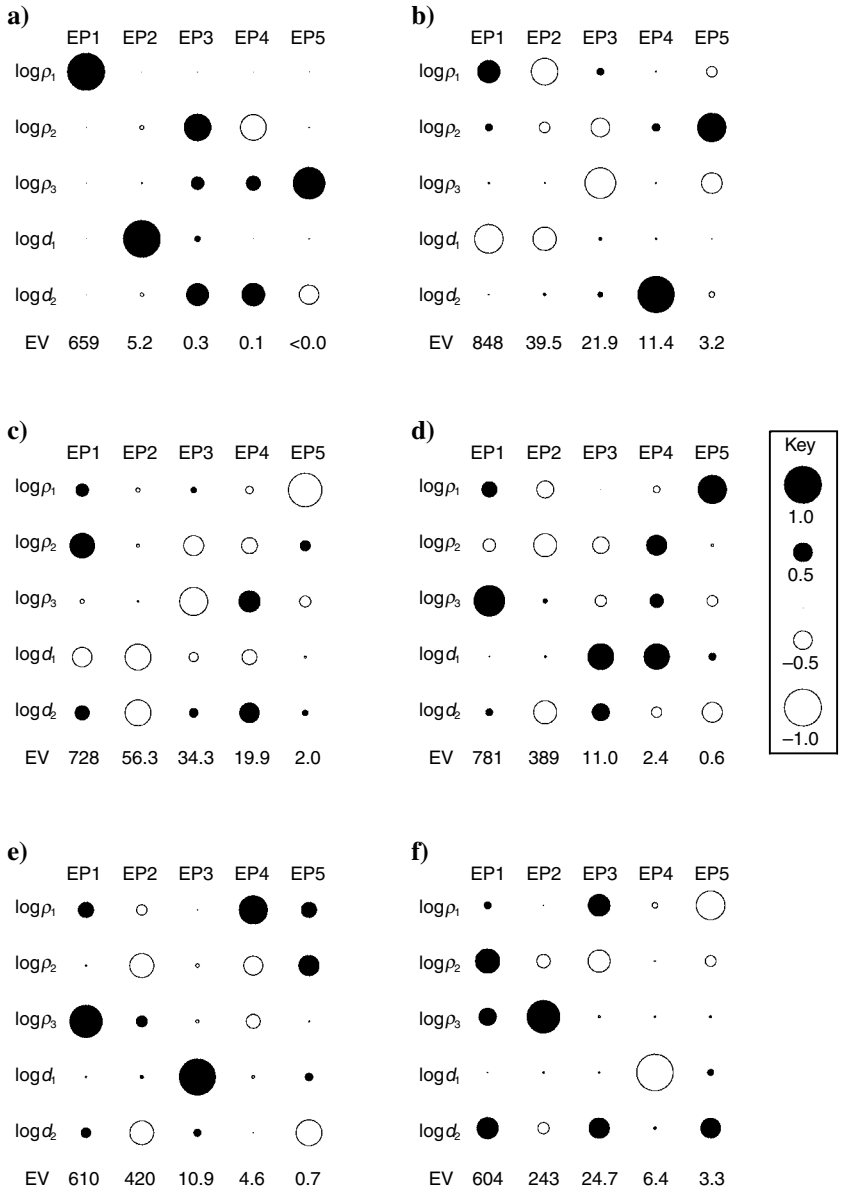


Figure 5. Eigenparameter (EPs) and eigenvalues (EVs) of the Jacobian for the three-layer model from Figure 1 and unit dipoles. (a–c) Results for the standard seafloor array with E_x-RX simulated at (a) $x = 50$, (b) 300, and (c) 900 m. (d–f) Results for the E_r-transients simulated at (d) $x = 50$, (e) 300, and (f) 900 m.

Downloaded 09/23/13 to 128.83.63.20. Redistribution subject to SEG license or copyright; see Terms of Use at http://library.seg.org/

For the downhole case (Figure 5d-f), the decrease in EVs is less significant than for the seafloor array, indicating that more parameters might be resolved. However, most EPs represent combinations of many model parameters, which might lead to ambiguous interpretations. In general, ρ_3 is far more important, since the TX is embedded in layer 3. Least important is d_1 because this parameter does not change the integrated resistivity between the TX and RX levels because $\rho_1 = \rho_3$. The structure of the EPs is similar for all offsets, in particular for the first two RXs. The result for the RX at 900-m offset is not very different from the one for the standard seafloor array.

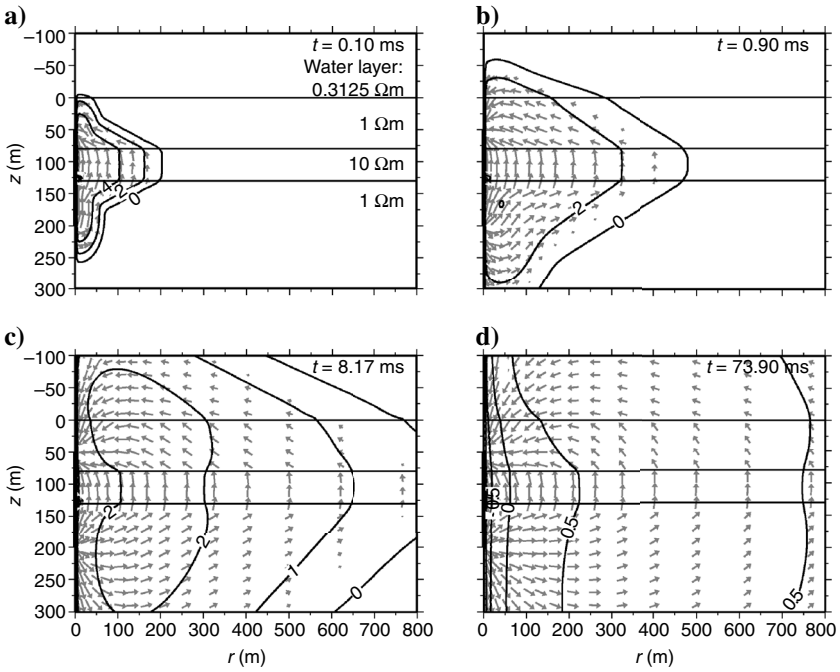


Figure 6. Evolution of the switch-on fields for an extended downhole E_z-TX for the three-layer case.

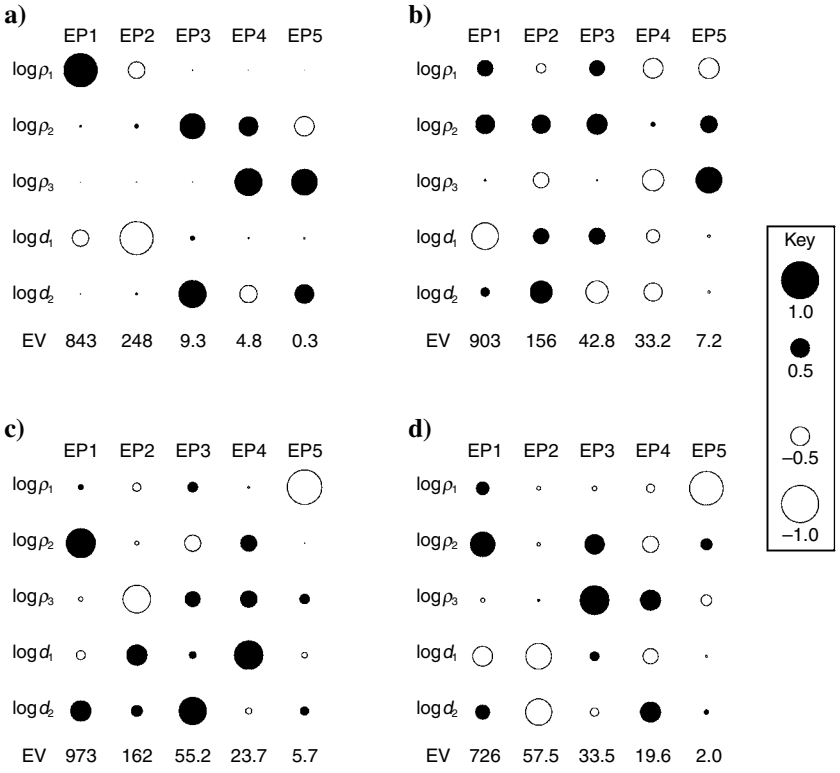


Figure 7. Eigenparameter and eigenvalues of the Jacobian for extended transmitters. (a–c) Results for the E_r transients simulated at (a) $x = 50$, (b) 300, and (c) 900 m. (d) Results for E_x transients simulated at $x = 900$ m.

Up to this point, we have considered only unit dipoles. In order to achieve measurable signal strengths, extended bipole antennas would typically be used. In the case of the inline array, this setup does not change the resolution significantly because the basic TX-RX-layer geometry is not changed. For the downhole TX, this is not the case.

In the next model calculations, we consider transmitting dipoles of 150-m length. The midpoints of the extended dipoles are located at $x = y = 0$ m and $z = 0$ m (seafloor, E_x-TX) or $z = 125$ m depth (E_z-TX). For the downhole TX, this geometry means that the electrodes are at depths of 50 and 200 mbsf, respectively. Hence, the TX dipole penetrates the target layer. Figure 6 shows the field disturbances produced by the extended downhole TX, normalized by the TX dipole moment.

The eigenparameter analyses for the downhole components (Figure 7a-c) show properties very similar to those of the E_x transients in Figure 5a-c, but the EVs decay less significantly. For the second and third E_r-RX, all eigenvalues are at least 1% of the largest. Of course, the influence of the deeper structure at short offsets is significantly smaller than with the short, deep TX because a smaller fraction of the TX is situated in the deep medium. Choosing a certain TX extension, depending on the target layer's depth and thickness, thus makes it possible to optimize the resolution of certain model parameters. As expected, the resolution for the inline data sets does not change significantly (Figure 7d).

RESOLUTION OF LATERAL CHANGES

The obvious drawback of the downhole TX is that a borehole is needed. The additional effort to deploy RX units and a downhole TX can only be justified if, in addition to borehole properties, lateral changes with r and ϕ can also be detected.

We used the time-domain forward-modeling code by (Druskin and Knizhnerman, 1988, 1994; Hördt et al., 1992; Druskin et al., 1999). The code is based on the spectral Lanczos decomposition method to solve the diffusion equation with a finite-difference approach.

Figure 8a-d shows fields produced by an extended vertical dipole TX. The geometry is the same as in the layered case shown in Figure 6. The resistive layer, however, is replaced by a re-

Downloaded 09/23/13 to 128.83.63.20. Redistribution subject to SEG license or copyright; see Terms of Use at http://library.seg.org/

sistive block with the same thickness and lateral extensions of $-3 \le y \le 3$ km and $-3 \le x \le 0.35$ km. The fields are similar to the 1D case until the field disturbances reach the end of the resistor. From that point on, the field disturbance diffuses more slowly because of the lower resistivity at the target depth.

Figure 8e-h shows the difference between the 3D model electric field and the layered case. For clarity's sake, the electric-field difference arrows are scaled differently from those of the total field, and thus their lengths cannot be compared directly.

Differences appear after the field disturbance reaches the end of the block and spreads out with increasing time. Deviations are largest shortly beyond the end of the block at around x = 450 m. Closer to the TX, the differences are smaller because the difference in the resistivity structure is smaller. For increasing offsets, the differences decrease with total field strength. For $x < 400$ m, the difference in the radial electric-field component at the seafloor is negative, and it is negative for $x > 500$. The difference in the vertical electric field is maximal shortly behind the lateral discontinuity.

Figure 9a-d the shows the evolution of the fields for a different resistivity model. Here, the resistive layer is thicker for $150 < x < 250$ m. Figure 9e-h shows the differences between the electric fields calculated for the two 3D models. At around 150-m offset, a maximum in the difference in the vertical component measured at the seafloor is found. The second lateral change at x = 350 m correlates with a sign reversal in the vertical component of the difference vector. The plots show a maximum of the anomalous field system at around 8 ms (Figure 9f). The effect can also be observed in Figure 8g and h.

DISCUSSION

Our model studies indicate that the most important factor in determining resolution is not the orientation of the TX, but the relative positions of TX, RX, and the target. For example, the curves calculated for horizontal and vertical dipole TXs at the seafloor show the same arrival times (Figure 4c) because the vertical distance to the target layer and the relevant diffusion properties of the medium are identical in both scenarios.

Resolution of the parameters of a layered model is similar for both configurations at offsets that are large with respect to the target's depth and, in case of a vertical dipole, the depth of the TX. In both cases, the data mainly resolve combinations of parameters, so that if no additional information about the shallower structure is available, the interpretation can be ambiguous.

If TX and RX are above the target, this additional information is provided by the data recorded at short offsets because it is not influenced significantly by deeper structures. Hence, vertical resolution is much improved by using several TX-RX offsets in the seafloor inline array. Nevertheless, this also is the biggest drawback of this configuration. Lateral and vertical resistivity changes cannot easily be separated and require several TX-RX positions. Further, the signal decays with offset, so it might not be detectable at the offset needed to resolve the layer.

For the case of an E_z-TX below the target layer, the transient shape is influenced by the resistivity structure between the TX and the seafloor, even at short offsets. However, not all model parameters can be resolved independently by using data from a single RX. Instead, significant EPs are formed of combinations of parameters. In particular,

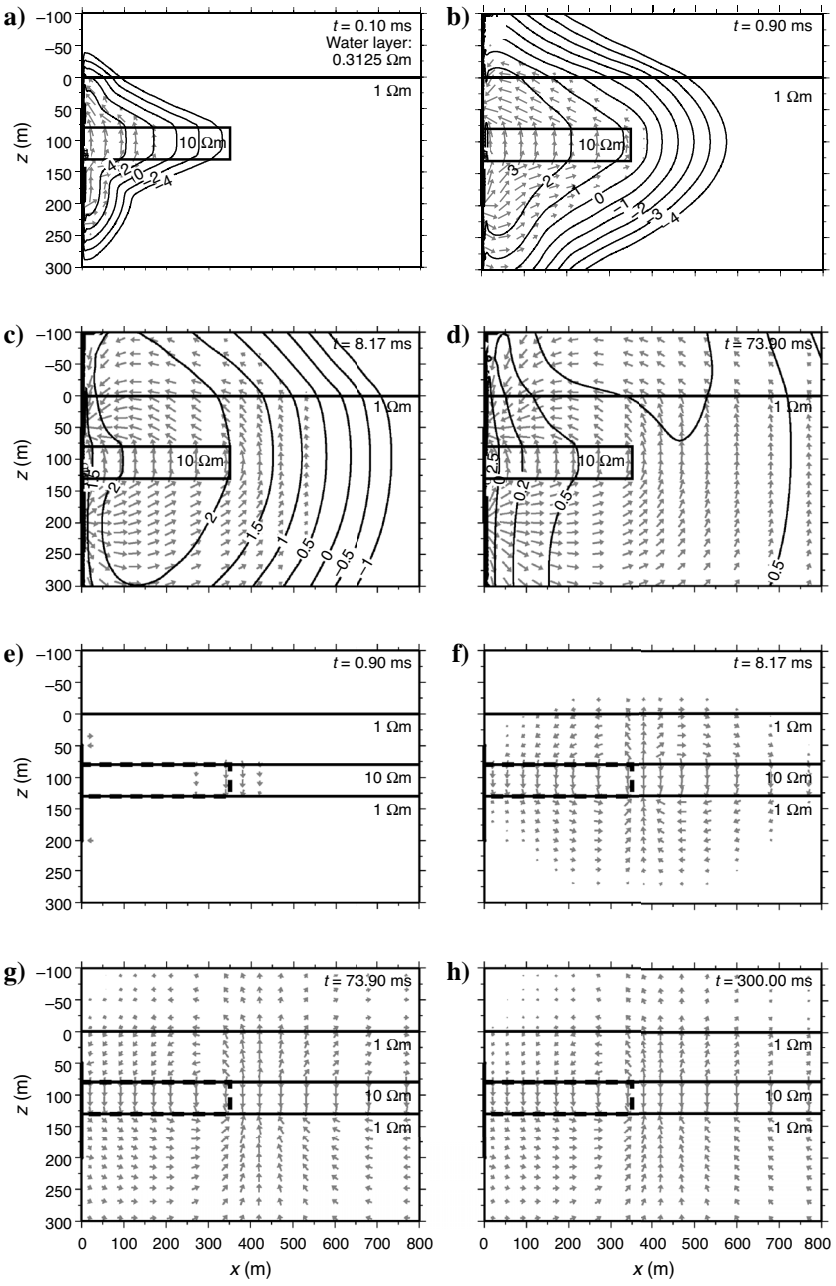


Figure 8. Evolution of switch-on fields at y = 0 km for an extended downhole E_z-TX. (a–d) Fields for a 3D model. (e–h) Difference of the electric fields between the 3D model (dashed lines) and the 1D three-layer case.

the vertical distribution of these resistivities is not well resolved. Still, more information can be derived from the downhole TX data than for the seafloor array, especially at short offsets. Compared to the seafloor array, additional separations provide less improvement in vertical resolution, because the resolution properties vary little with increasing offset.

Resolution can be increased by extending the TX dipole significantly above the target layer. Part of the signal reaches the RX at the seafloor without passing through the target. Resolution properties appear to be a mixture of those of the seafloor array and the downhole-to-seafloor geometry.

We did not explicitly investigate the effect of extending the TX dipole when the target is a finite body. It can be expected that the resolution of the body decreases with the ratio of dipole length and lateral extension of the target. We propose to use multiple electrodes in one or more boreholes, to be able to switch through different TX configurations similar to arrays commonly used in land-based, crosshole applications.

It might be better to reverse the TX-RX setup, i.e., to put E_z receivers down a borehole and drag an electric dipole of several hundred meters length along the seafloor. An advantage of this setup is that the transmitter's dipole moment can be increased more easily if needed. Following the reciprocity theorem, this setup will result in the same transients. Multiple E_z receivers at different depths will aid in resolving the model parameters independently, comparable to downhole-TX examples using extended dipoles.

Multidimensional modeling gives insight into the evolution of downhole-TX fields in more complex settings. Electric-field differences between a reference model and a 3D model showed a nice correlation to lateral resistivity changes. Resolving these features from seafloor measurements would require multiple TX and RX locations and sufficiently large targets.

One advantage of the downhole TX is that it does not excite an airwave. However, according to reciprocity, the same results can be obtained by a horizontal transmitter and vertical E_z receivers.

All model calculations of this study were carried out under the assumption of no metal casing in the borehole. If a casing is present, the fields may be distorted severely to the point where no useful information about the outside resistivity structure can be derived.

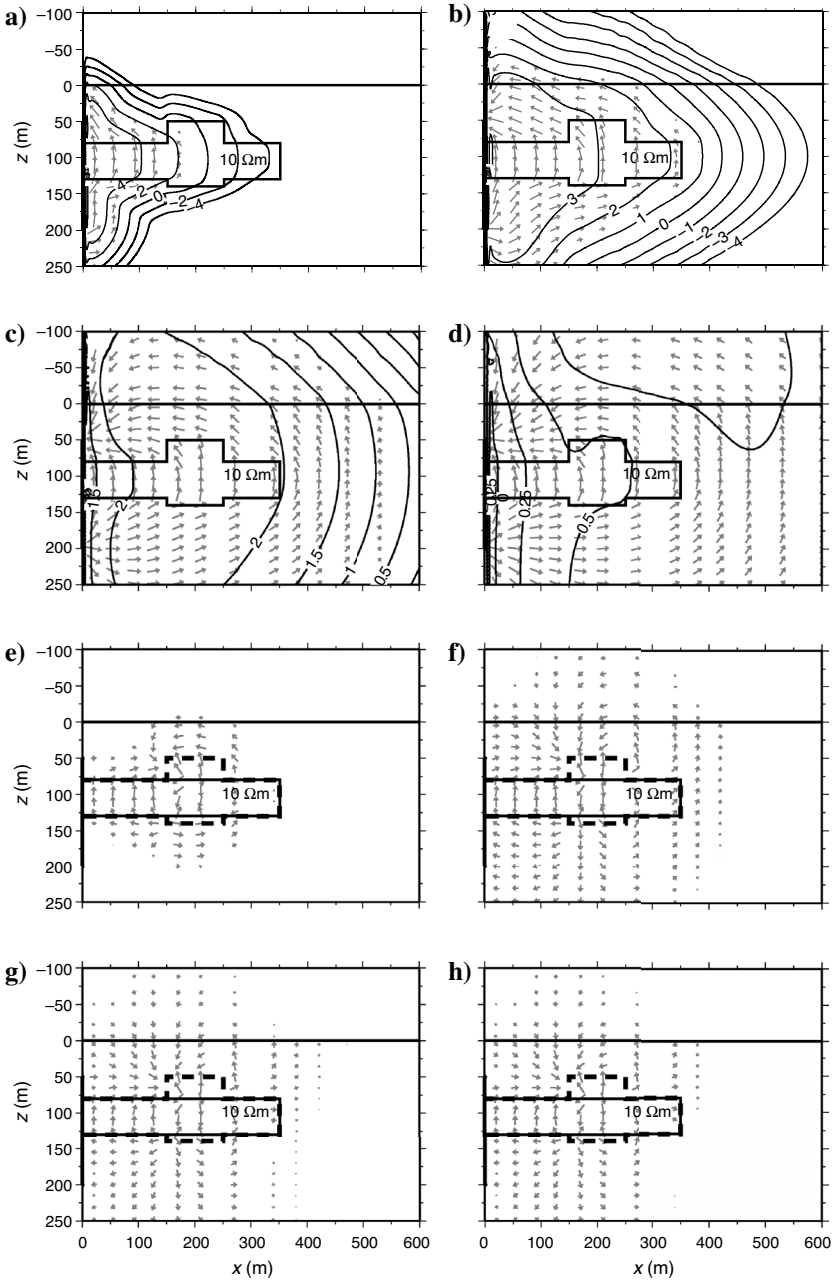


Figure 9. Evolution of switch-on fields at $y = 0$ km for an extended downhole E_z-TX. (a–d) Fields for a 3D model. (e–h) Difference of the electric fields between the 3D model (dashed lines) and the 3D model used in Figure 8.

CONCLUSIONS

The objective of this research was to compare the relative merits of a vertical-electric dipole TX in a borehole and a standard seafloor array. To study the resolution of a resistive target layer, we derived solutions to field equations for this transmitter in a conductive medium.

If we assume that the RX arrays for both TX types are extended to appropriate offsets, the downhole-to-seafloor array appears to have a superior lateral but poorer vertical resolution. In both cases, the resolution can be improved by using different TX positions. Using both configurations will aid in constraining the resistivity model because the resolution properties are different for the two setups, in particular for the area close to the borehole. Ideally, a survey would be carried out by using both downhole and seafloor components to establish an initial resistivity model. Thereafter, the downhole configuration would be well suited for monitoring purposes because of the good lateral resolution when only one stationary TX dipole is used.

Downloaded 09/23/13 to 128.83.63.20. Redistribution subject to SEG license or copyright; see Terms of Use at http://library.seg.org/

Downloaded 09/23/13 to 128.83.63.20. Redistribution subject to SEG license or copyright; see Terms of Use at http://library.seg.org/

ACKNOWLEDGMENTS

The Institute of Geophysics and Meteorology at the University of Cologne kindly provided the 3D forward code and appropriate computer facilities to use it. The experimental marine electromagnetic group at the University of Toronto is supported by grants from the Natural Sciences and Engineering Research Council of Canada. We thank Ele Willoughby, Rob Evans, Kurt Strack, and Michael Wilt for useful commentaries on the paper.

APPENDIX A

THE VERTICAL DIPOLE IN A LAYERED EARTH

We wish to know the electric and magnetic fields of a vertical electric dipole having a strength of $I\Delta \exp(i\omega t)$ buried in a layered earth and grounded to it by a pair of electrodes as shown in Figure A-1. The center of the dipole is at the origin O of cylindrical coordinates (r, ϕ, z). It is within a very thin layer of thickness Δ that has a resistivity ρ_0. The resistivities and thicknesses of N layers below the source layer and M layers above it are denoted by subscripts i and j on symbols ρ and d, respectively. Indices i and j increase away from the source, starting from unity.

There are two typical field points F_i and F_j also located at layer interfaces, between the ith and $(i + 1)$th and the jth and $(j + 1)$th layers below and above the source, respectively.

The problem is axisymmetric. The one and only azimuthal magnetic component B_ϕ satisfies the Helmholtz differential equation:

$$\frac{\partial^2 B_\phi}{\partial r^2} + \frac{1}{r}\frac{\partial B_\phi}{\partial r} - \frac{B_\phi}{r^2} + \frac{\partial^2 B_\phi}{\partial z^2} = \alpha^2 B_\phi, \qquad \text{(A-1)}$$

where $\alpha^2 = i\omega\mu_0/\rho$, at all source-free points within zones of constant resistivity. A Hankel transform pair relating any two functions $A(r;z)$ and $A(\lambda;z)$, may be defined as

$$A(\lambda;z) = \int_0^\infty rA(r;z)J_1(\lambda r)dr \qquad \text{(A-2)}$$

and

$$A(r;z) = \int_0^\infty \lambda A(\lambda;z)J_1(\lambda r)d\lambda, \qquad \text{(A-3)}$$

where J_1 is a Bessel function of the first kind of order one. The Hankel transform of the partial differential equation A-1 yields the simple second-order equation

$$\frac{d^2 B_\phi}{dz^2} - \theta^2 B_\phi = 0, \qquad \text{(A-4)}$$

where $\theta^2 = \lambda^2 + \alpha^2$. A solution of differential equation A-4 in any lower layer i, of constant resistivity ρ_i and thickness d_i, is

$$B_{\phi,i}(\lambda;z) = U[\cosh(\theta_i z) + V\sinh(\theta_i z)], \qquad \text{(A-5)}$$

where U and V are functions independent of z constrained by the boundary conditions.

As the current flow is continuous everywhere, the radial electric-field component is related to the magnetic component (equation A-5) by Ampere's law $E_r = -(\rho/\mu_0)dB_\phi/dz$, so that

$$\mu E_{r,i}(\lambda;z) = -\theta\rho_i U[\sinh(\theta_i z) + V\cosh(\theta_i z)]. \qquad \text{(A-6)}$$

Eliminating U and V from equations A-5 and A-6 and rearranging generates an upward recursion relationship,

$$Q_i(\lambda) = \frac{1}{\rho_i\theta_i}\left[\frac{\rho_i\theta_i Q_{i+1} + \tanh(\theta_i d_i)}{\rho_i\theta_i Q_{i+1}\tanh(\theta_i d_i) + 1}\right], \qquad \text{(A-7)}$$

where the symbol Q denotes the ratio $B_\phi/\mu E_r$ and Q_i and Q_{i+1} are the specific values of Q at the top and bottom of the ith layer. For any given λ, the value of Q just below the source layer Q_1 can be obtained by successive applications of expression A-7 from a starting value at the top of the lower half-space given by

$$Q_N = 1/(\rho_N\theta_N). \qquad \text{(A-8)}$$

A solution of differential equation A-4 in any upper layer j above the source also is

$$B_{\phi,j}(\lambda;z) = U[\cosh(\theta_j z) + V\sinh(\theta_j z)], \qquad \text{(A-9)}$$

and the radial electric component is

$$\mu_0 E_{r,j}\lambda;z) = -\theta_j\rho_j U[\sinh(\theta_j z) + V\cosh(\theta_j z)]. \qquad \text{(A-10)}$$

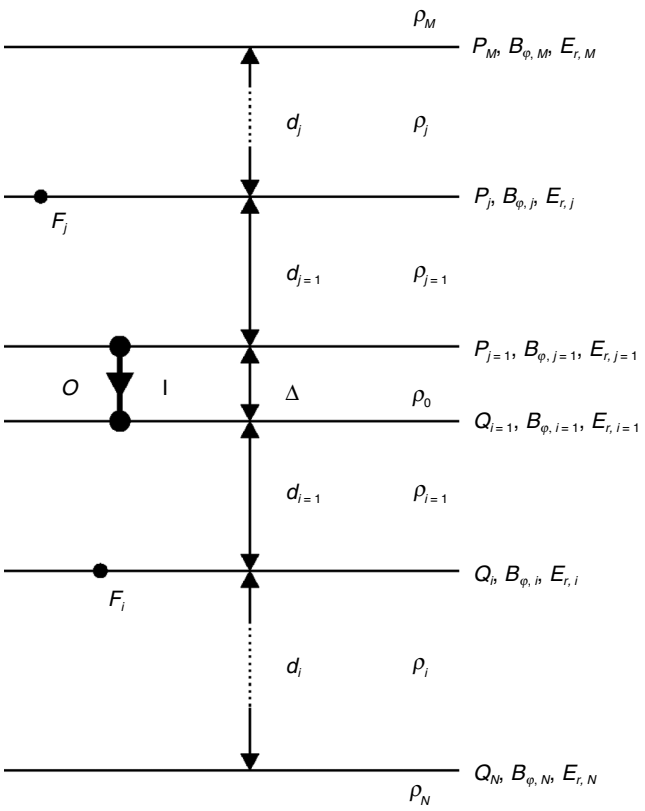


Figure A-1. Sketch of the geometry for derivation of the fields of a vertical dipole at the origin O.

Downloaded 09/23/13 to 128.83.63.20. Redistribution subject to SEG license or copyright; see Terms of Use at http://library.seg.org/

Eliminating U and V from equations A-9 and A-10 gives the downward recursion relationship

$$P_j(\lambda) = \frac{1}{\rho_j\theta_j}\left[\frac{\rho_j\theta_j P_{j+1} + \tanh(\theta_j d_j)}{\rho_j\theta_j P_{j+1}\tanh(\theta_j d_j) + 1}\right], \quad \text{(A-11)}$$

where the symbol P denotes the ratio $-B_\phi/\mu E_r$, and P_j and P_{j+1} are the specific values of P at the bottom and top of the jth layer. For any given λ, the value of P just above the source layer P_1 can be obtained by successive applications of expression A-11 from a starting value

$$P_M = 1/(\rho_M\theta_M). \quad \text{(A-12)}$$

The value of P_M approaches zero if the upper half-space is air. In our algorithm, the air is discretized as half-space with a resistivity of 10^8 Ωm. The functions P and Q are continuous across all layer boundaries in regions above and below the source, respectively, but they are discontinuous across the source layer because of the effect of the current dipole. The magnetic field $B_{\phi,1}$ is continuous through the source layer, but the radial electric field E_r is not, because of the effects of the source. From the definitions of Q and P, the amount δE_r by which E_r below the source layer exceeds the value above may be written as

$$\delta E_r(\lambda) = \frac{B_{\phi,1}}{\mu_0}\left[\frac{P_1 + Q_1}{P_1 Q_1}\right]. \quad \text{(A-13)}$$

The magnetic field of a current dipole in a medium of resistivity ρ_0 is given by Wait (1982) and other texts as

$$B^s_\phi(r;z) = \frac{\mu_0 I\Delta r}{4\pi R^3}(1 + \alpha_0 R)\exp(-\alpha_0 R), \quad \text{(A-14)}$$

where $R^2 = r^2 + z^2$. Standard integrals listed in Chave and Cox (1982) may be used to convert equation A-14 to the Hankel integral

$$B^s_\phi(\lambda;z) = \frac{\mu_0 I\Delta}{4\pi}\int_0^\infty (\lambda^2/\theta_0) \times\exp(-\theta_0|z|)J_1(\lambda r)d\lambda. \quad \text{(A-15)}$$

The Hankel transform $B^s_\phi(\lambda)$ of $B^s_\phi(r)$ is by inspection

$$B^s_\phi(\lambda) = \frac{\mu_0 I\Delta}{4\pi}(\lambda/\theta_0)\exp(-\theta_0|z|). \quad \text{(A-16)}$$

The transforms of the radial electric fields may be obtained through Ampere's law, and the discontinuity δE^s_r across the layer may be evaluated as

$$\delta E^s_r(\lambda) = \frac{\rho_0 I\Delta\lambda}{2\pi}. \quad \text{(A-17)}$$

If equations A-13 and A-17 are equated, an expression for $B_{\phi,1}(\lambda)$ in terms of the layered structure is obtained as

$$B_{\phi,1}(\lambda) = \frac{\mu_0\rho_0\lambda I\Delta}{2\pi}\left[\frac{P_1 Q_1}{P_1 + Q_1}\right]. \quad \text{(A-18)}$$

A consistency check can be applied by assuming that there is only one layer above the source and one layer below the source of resistivity ρ_0. Then, $P_1 = Q_1 = 1/(\theta_0\rho_0)$, and the value of $B_{\phi,1}$ is

$$B_{\phi,1}(\lambda) = \frac{\mu_0 I\Delta}{4\pi}(\lambda/\theta_0), \quad \text{(A-19)}$$

which is consistent with equation A-16 for $z = 0$.

The fields at the typical observation points F_i or F_j may now be computed by downward- or upward-recursion rules, respectively, which start with $B_{\phi,1}$. The downward recursion rule through the ith layer may be derived from equations A-5 and A-6 as

$$B_{\phi,i+1}(\lambda) = \left[\frac{\rho_i\theta_i Q_{i+1}\mathrm{sech}(\theta_i d_i)}{\rho_i\theta_i Q_{i+1} + \tanh(\theta_i d_i)}\right]B_{\phi,i}(\lambda). \quad \text{(A-20)}$$

The values of Q needed by the rule are saved values from the preceding upward-recursion process. The algorithm avoids the evaluation of exponentials with positive arguments.

The upward-recursion rule through the jth layer may be derived in a similar manner from equations A-9 and A-10 as

$$B_{\phi,j+1}(\lambda) = \left[\frac{\rho_j\theta_j P_{j+1}\mathrm{sech}(\theta_j d_j)}{\rho_j\theta_j P_{j+1} + \tanh(\theta_j d_j)}\right]B_{\phi,j}(\lambda). \quad \text{(A-21)}$$

The Hankel transform of the radial electric field is obtained from the magnetic field at the field points through the use the local values of Q_i and P_j, respectively. The final evaluation of the fields B_ϕ and E_r at F_i and F_j in the space domain is through the inverse Hankel transform equation A-3.

The vertical current density $J_z(r)$, continuous across all layers except the source layer, is obtained from the space-domain integral for $B_\phi(r)$ by Ampere's law,

$$J_z(r) = (1/\mu_0)\frac{1}{r}\frac{\partial}{\partial r}rB_\phi(r), \quad \text{(A-22)}$$

which leads to a zero-order Hankel transform. The vertical electric component E_z is discontinuous across layer boundaries and is evaluated above or below a layer boundary as the product of J_z with the appropriate resistivity.

The fields are derived for point dipoles. To calculate the fields for physical, extended dipoles, the fields are simulated and integrated for several point dipoles.

To observe diffusion of the current systems away from the transmitter, we prefer to watch the fields in the time domain. The transformation requires the calculation for several frequencies and the use of a fast Hankel transform of a half-integer order (Johansen and Sorensen, 1979).

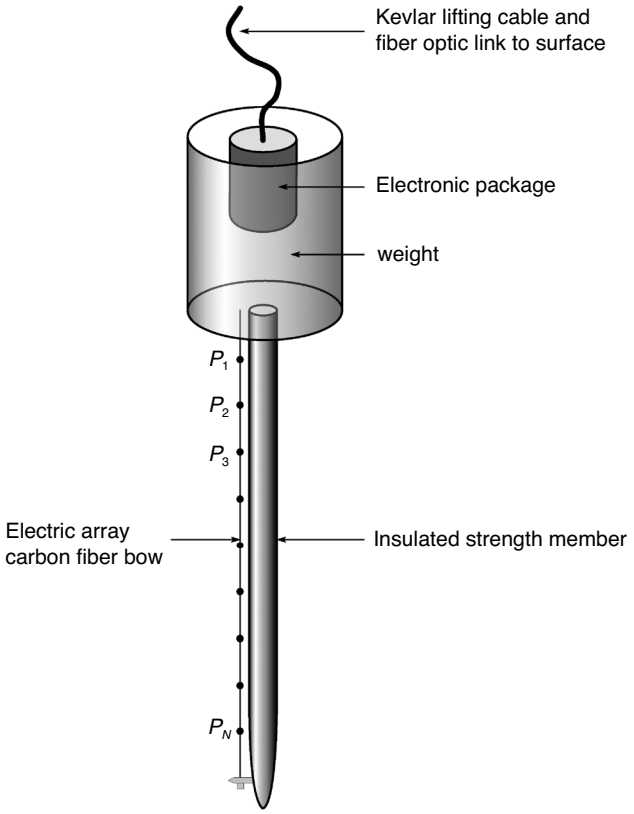


Figure A-2. Sketch of a modified heat-flow probe to measure the vertical electric field component E_z. Instead of thermistors, multiple potential electrodes are attached to the bow. The latter should be insulated or made from nonconductive material.

The horizontal-field components E_r and $\dot{B}_\phi$ can be measured with standard sensors. We propose to measure the vertical electric field E_z with a modified heat-flow probe (Figure A-2). The probe can be used in pogo-style deployments.

REFERENCES

Amundsen, H. E. F., S. Johansen, and T. Rosten, 2004, A sea bed logging (SBL) calibration survey over the troll gas field: Presented at the 66th Annual Conference and Exhibition, EAGE.

Chave, A. D., S. C. Constable, and R. N. Edwards, 1991, Electrical exploration methods for the seafloor, *in* M. N. Nabighian, ed.. Electromagnetic methods in applied geophysics, 2nd ed.: SEG, 931–966.

Chave, A. D., and C. S. Cox, 1982, Controlled electromagnetic sources for measuring the electrical conductivity beneath the oceans: Journal of Geophysical Research, **87**, 5327–5338.

Cheesman, S. J., R. N. Edwards, and A. D. Chave, 1987, On the theory of seafloor conductivity mapping using transient electromagnetic systems: Geophysics, **52**, 204–217.

Constable, S. C., and C. S. Cox, 1996, Marine controlled-source electromagnetic sounding, 2, The PEGASUS experiment: Journal of Geophysical Research, **101**, 5519–5530.

Druskin, V. L., and L. A. Knizhnerman, 1988, A spectral semi-discrete method for the numerical solution of 3D-nonstationary problems in electrical prospecting: Physics of the Solid Earth, **24**, 641–648.

———, 1994, Spectral approach to solving three-dimensional Maxwell's diffusion equations in the time and frequency domains: Radio Science, **29**, 937–953.

Druskin, V. L., L. A. Knizhnerman, and P. Lee, 1999, New spectral Lanczos decomposition method for induction modeling in arbitrary 3-D geometry: Geophysics, **64**, 701–706.

Edwards, R. N., 1988, Two-dimensional modeling of a towed in-line electric dipole-dipole sea-floor electromagnetic system — The optimum time delay or frequency for target resolution: Geophysics, **53**, 846–853.

———, 1997, On the resource evaluation of marine gas hydrate deposits using sea-floor transient electric dipole-dipole methods: Geophysics, **62**, 63–74.

Ellingsrud, S., T. Eidesmo, S. Johansen, M. Sinha, L. MacGregor, and S. Constable, 2002, Remote sensing of hydrocarbon layers by seabed logging (SBL): Results from a cruise offshore Angola: The Leading Edge, **21**, 972–982.

Hordt, A., V. L. Druskin, L. Knizhnerman, and K. M. Strack, 1992, Interpretation of 3-D effects in long-offset transient electromagnetic (LOTeM) soundings in the Munsterland area, Germany: Geophysics, **57**, 1127–1137.

Johansen, H. K., and K. Sorensen, 1979, Fast Hankel transforms: Geophysical Prospecting, **27**, 876–901.

Jupp, D. L. B., and K. Vozoff, 1975, Stable iterative methods for the inversion of geophysical data: Geophysical Journal of the Royal Astronomical Society, **42**, 957–976.

MacGregor, L., D. Andreis, J. Tomlinson, and N. Barker, 2006, Controlled-source electromagnetic imaging on the Nuggets-1 reservoir: The Leading Edge, **25**, 984–992.

Raiche, A. P., D. L.B. Jupp, H. Rutter, and K. Vozoff, 1985, The joint use of coincident loop transient electromagnetic and Schlumberger sounding to resolve layered structures: Geophysics, **50**, 1618–1627.

Riedel, M., G. D. Spence, N. R. Chapman, and R. D. Hyndman, 2002, Seismic investigations of a vent field associated with gas hydrates, offshore Vancouver Island: Journal of Geophysical Research, **107**, 2200.

Schwalenberg, K., E. Willoughby, R. Mir, and R. N. Edwards, 2005, Marine gas hydrate electromagnetic signatures in Cascadia and their correlation with seismic blank zones: First Break, **23**, 47–63.

Srnka, L., J. J. Carazzone, and M. S. Ephron, 2006, Remote reservoir resistivity mapping: The Leading Edge, **25**, 972–975.

Wait, J. R., 1982, Geo-electromagnetism: Academic Press.

Weitemeyer, K., S. Constable, and K. Key, 2006, Marine EM techniques for gas-hydrate detection and hazard mitigation: The Leading Edge, **25**, 629–632.

Yuan, J., and R. N. Edwards, 2000, The assessment of marine gas hydrate through electrial remote sounding electrical remote sounding: Hydrate without a BSR?: Geophysical Research Letters, **27**, 2397–2400.

Downloaded 09/23/13 to 128.83.63.20. Redistribution subject to SEG license or copyright; see Terms of Use at http://library.seg.org/